

# Imaging spectroscopy of albedo and radiative forcing by light-absorbing impurities in mountain snow

Thomas H. Painter,<sup>1,2</sup> Felix C. Seidel,<sup>1</sup> Ann C. Bryant,<sup>3</sup> S. McKenzie Skiles,<sup>2</sup> and Karl Rittger<sup>1</sup>

Received 24 December 2012; revised 25 March 2013; accepted 23 May 2013; published 5 September 2013.

[1] Recent studies show that deposition of dust and black carbon to snow and ice accelerates snowmelt and perturbs regional climate and hydrologic cycles. Radiative forcing by aerosols is often neglected in climate and hydrological models in part due to scarcity of observations. Here we describe and validate an algorithm suite (Imaging Spectrometer-Snow Albedo and Radiative Forcing (IS-SnARF)) that provides quantitative retrievals of snow grain size, snow albedo, and radiative forcing by light-absorbing impurities in snow and ice (LAISI) from Airborne Visible/Infrared Imaging Spectrometer (AVIRIS) data collected on 15 June 2011 in the Senator Beck Basin Study Area (SBBBA), SW Colorado, USA. Radiative forcing by LAISI is retrieved by the integral of the convolution of spectral irradiance with spectral differences between the spectral albedo (scaled from the observed hemispherical-directional reflectance factor (HDRF)) and modeled clean snow spectral albedo. The modeled surface irradiance at time of acquisition at test sites was  $1052 \text{ W m}^{-2}$  compared to  $1048 \text{ W m}^{-2}$  measured with the field spectroradiometer measurements, a relative difference of 0.4%. HDRF retrievals at snow and bare soil sites had mean errors relative to in situ measurements of  $-0.4 \pm 0.1\%$  reflectance averaged across the spectrum and root-mean-square errors of  $1.5 \pm 0.1\%$ . Comparisons of snow albedo and radiative forcing retrievals from AVIRIS with in situ measurements in SBBBA showed errors of  $0.001\text{--}0.004$  and  $2.1 \pm 5.1 \text{ W m}^{-2}$ , respectively. A counterintuitive result was that, in the presence of light absorbing impurities, near-surface snow grain size increased with elevation, whereas we generally expect that at lower elevation the grain size would be larger.

**Citation:** Painter, T. H., F. C. Seidel, A. C. Bryant, S. McKenzie Skiles, and K. Rittger (2013), Imaging spectroscopy of albedo and radiative forcing by light-absorbing impurities in mountain snow, *J. Geophys. Res. Atmos.*, **118**, 9511–9523, doi:10.1002/jgrd.50520.

## 1. Introduction

[2] Deposition of light-absorbing impurities, such as mineral dust and carbonaceous particles, to mountain snow cover has been increasing in many mountain ranges of the globe across the last two centuries—the Anthropocene [Zalasiewicz *et al.*, 2010]. Dust from disturbed arid and semi-arid lands has increased several fold within this period in the Rocky Mountains [Neff *et al.*, 2008; Reynolds *et al.*, 2009], the Himalaya [Thompson *et al.*, 2000], the Caucasus Mountains [Davitaya, 1968], and the Antarctic Peninsula [McConnell *et al.*, 2007]. With industrialization and increases in biomass burning with increasing population, deposition of carbonaceous particles (i.e., black carbon and brown carbon) to

mountain snow such as the Himalaya and the Alps has likewise increased several fold [Thevenon *et al.*, 2009; Zalasiewicz *et al.*, 2010; Kaspari *et al.*, 2011]. When at or near the snow-atmosphere interface, these light-absorbing impurities in snow and ice (LAISI) necessarily decrease snow spectral albedo and in turn accelerate snow warming and melt, contributing to the snow-albedo feedback.

[3] Recent studies have shown from detailed in situ measurements in the Upper Colorado River basin that the additional absorbed solar radiation by LAISI (radiative forcing) ranges from  $31$  to  $75 \text{ W m}^{-2}$ , accelerating snowmelt such that snow cover is shortened by 26–50 days [Painter *et al.*, 2007b; Painter *et al.*, 2012b; Skiles *et al.*, 2012]. Extrapolating these point measurements to the entire Upper Colorado River basin suggests that the several fold increase in dust loading and reduction in snow albedo from the pre-1800s background load bring peak runoff at Lee's Ferry, Arizona, 3 weeks earlier and decrease annual runoff by an average of 5% [Painter *et al.*, 2010]. Model simulations of the Himalaya to Tibetan Plateau likewise suggest that radiative forcing by black carbon through atmospheric heating and increased net solar radiation at the snow surface reaches  $5\text{--}25 \text{ W m}^{-2}$ , resulting in four times more powerful impact on snowmelt than the increase in air temperature from the

<sup>1</sup>Jet Propulsion Laboratory, California Institute of Technology, Pasadena, California, USA.

<sup>2</sup>Joint Institute for Regional Earth System Science and Engineering, University of California, Los Angeles, California, USA.

<sup>3</sup>Department of Geography, University of Utah, Salt Lake City, Utah, USA.

Corresponding author: T. H. Painter, Jet Propulsion Laboratory, California Institute of Technology, Pasadena, CA 91109. (thomas.painter@jpl.nasa.gov)

©2013. American Geophysical Union. All Rights Reserved.  
2169-897X/13/10.1002/jgrd.50520

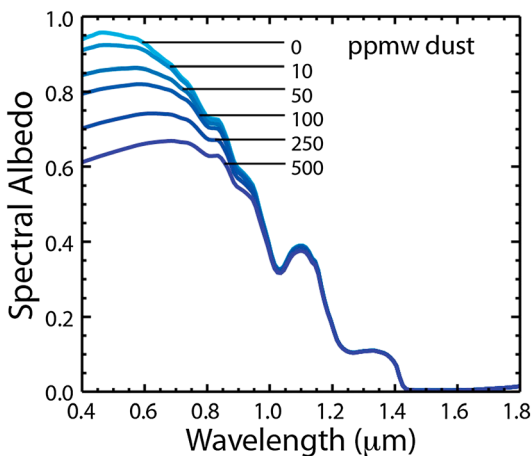


**Figure 1.** Model simulations of spectral albedo of clean snow and dust-laden snow of the same optical grain radius for varying concentrations of dust, highlighting the continuous variation of the impact of impurities on spectral albedo with variation in concentration.

preindustrial to present increase in atmospheric CO<sub>2</sub> [Lau et al., 2010; Qian et al., 2011].

[4] All of these studies of LAISI impacting the surface energy balance were derived or validated by in situ measurements. No remotely sensed observations of radiative forcing by LAISI have been available until very recently with the introduction of the Moderate Resolution Imaging Spectroradiometer (MODIS) Dust Radiative Forcing in Snow (MODDRFS) model for multispectral polar-orbiting optical data [Painter et al., 2012a]. MODDRFS has a bias-corrected uncertainty of 32 W m<sup>-2</sup> and mean absolute error of 25 W m<sup>-2</sup> based on validation from the Senator Beck Basin Study Area, Colorado, USA. However, MODDRFS uncertainties come from the poor knowledge of where in the spectrum that the LAISI are impacting the spectral albedo, from which we determine the radiative forcing. The marked gaps in the spectrum not measured by MODIS are completely sampled by an imaging spectrometer. Additionally, the MODIS ground instantaneous field of view at nadir is 463 m, which results in the vast majority of mountain pixels being mixed with exposed rock and vegetation, rendering the MODDRFS more qualitative. Finally, the bias correction for MODDRFS is based on energy balance and radiation towers in the Colorado River basin and may well affect regional bias, still to be determined.

[5] To address the capacity to more quantitatively retrieve radiative forcing by LAISI from imaging spectrometer data, we have developed the Imaging Spectrometer-Snow Albedo and Radiative Forcing (IS-SnARF) model. This model is similar in structure to the MODDRFS model [Painter et al., 2012a] but uses the full spectrum of the imaging spectrometer to provide more robust retrievals. Here we present the retrieval of snow optical grain size (radius), albedo, and at-surface radiative forcing by LAISI from the Airborne Visible/Infrared Imaging Spectrometer (AVIRIS).

[6] We describe the foundations of snow albedo and radiative forcing by LAISI (section 2). In section 3, we describe the study region, in situ measurements, and the AVIRIS data. We then describe in section 4 the atmospheric characterization and reflectance retrieval, and retrieval of albedo and radiative

forcing. In sections 5 and 6, we present the AVIRIS results and a discussion of uncertainties and applications of the algorithm in future missions.

## 2. Background

[7] Net solar radiation is the main driver for melting snow in the mountains (except for dense to closed-canopy forest areas) [Oerlemans, 2000; Painter et al., 2007b], itself controlled by changes in spectral irradiance and snow albedo. Changes in irradiance are mainly controlled by the sunlight duration and intensity as a function of the time of year, topographic exposure, cloud cover, and atmospheric optical depth. Changes in clean snow albedo are controlled by fresh snowfall and snow metamorphism. The former increases the snow albedo, while the latter leads to increasing snow grain sizes and lower snow albedo. An even stronger decrease of snow albedo is given by the accumulation of LAISI.

[8] Increases in grain size decrease the spectral albedo in the near-infrared (0.7–1.5 μm) and shortwave-infrared wavelengths (1.5–3.0 μm). However, LAISI decrease the spectral snow albedo from 0.95–0.98 down to as low as 0.30 primarily in the visible part of the solar spectrum where approximately half of the incoming irradiance lies [Painter et al., 2012b]. Therefore, snow might have the greatest variability of albedo of any natural surface on Earth.

[9] The LAISI absorb solar radiation and primarily conduct that energy to heat the surrounding snow. Additional radiative forcing contributes to snowmelt once the temperature of the snowpack reaches the melting point. The timing and magnitude of radiative forcing are controlled by the deposition of LAISI and their persistence at or near the snow surface. Subsequent snowfall can bury LAISI deposited during early-to middle-winter storms, limiting the amount of time they spend at or near the snow surface-absorbing solar irradiance, whereas those that come later in the spring can more immediately increase absorption of sunlight.

[10] The particle size of LAISI is generally large enough that they are not entrained in snowmelt and washed to deeper layers [Higuchi and Nagoshi, 1977; Conway et al., 1996; Sterle et al., 2013]. Instead, water percolates from overlying snowmelt to below the impurity layer. With progressing melt, LAISI layers merge, increasing the LAISI concentration and decreasing the visible and near-infrared spectral albedo further [Painter et al., 2012b]. This leads to an even stronger snow albedo feedback with increasing radiative forcing and snowmelt. In some cases, smaller particles such as black carbon in isolation can be flushed to depth [Conway et al., 1996], and it is suggested that impurity hygroscopicity can influence percolation rates [Conway et al., 1996].

[11] Radiative forcing by LAISI is described in its direct effect and two feedback effects [Hansen and Nazarenko, 2004; Painter et al., 2012b]. The direct effect is the enhanced absorption of solar irradiance by the absorbing impurities themselves, primarily in the visible and near-infrared (Figure 1). The first indirect feedback is given by enhanced absorption of solar irradiance due to accelerated grain growth driven by the direct effect. The entire spectrum albedo is therefore influenced by increasing the direct absorption in the visible wavelengths and reinforcing the absorption by the larger absorbing path length in the near-infrared through shortwave-infrared (Figure 1). Finally, the second indirect feedback is given

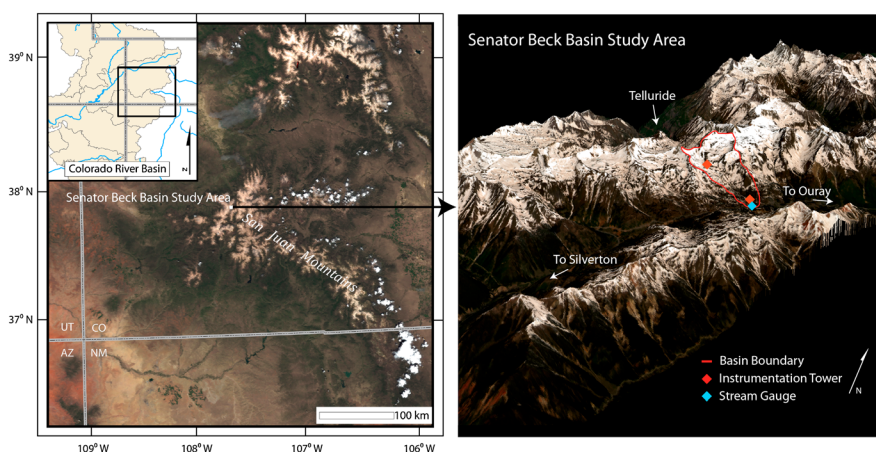


**Figure 2.** Overview of the study region—the Senator Beck Basin Study Area, Colorado, USA, and surrounding mountains.

when the darker substrate (i.e., soil, rock, and/or vegetation) is exposed by the earlier complete melt of snow cover driven by the direct and first indirect feedback. Here we focus the retrieval on the at-surface direct effect radiative forcing.

### 3. Site and Data

[12] In this paper, we present retrievals of snow optical grain radius, snow albedo, and radiative forcing by LAISI from data acquired with the NASA/Jet Propulsion Laboratory (JPL) Airborne Visible/Infrared Imaging Spectrometer (AVIRIS) over the San Juan Mountains, Colorado (Figure 2), on 15 June 2011, from the NASA ER-2 platform.

#### 3.1. Site

[13] The AVIRIS flight line lies approximately north-south in orientation across the Senator Beck Basin Study Area (SBBBA), western San Juan Mountains in the Upper Colorado River Basin ( $37^{\circ}54'30''\text{N}$ ,  $107^{\circ}43'30''\text{W}$ ). The SBBBA covers a generally east facing basin and is equipped with two micrometeorological stations measuring energy balance and radiation fluxes in the alpine and subalpine [Painter et al., 2012b; Skiles et al., 2012]. These two sites are unique in their generation of knowledge of snowmelt dynamics in the Colorado River Basin [Painter et al., 2012b].

#### 3.2. Remote-Sensing Data

[14] AVIRIS measures spectral radiance in the visible to shortwave infrared from 356 to 2512 nm in 224 contiguous channels of approximately 10 nm spectral sampling interval, an instantaneous field of view (IFOV) of 1 mrad, and field of view of  $34^{\circ}$  ( $\pm 17^{\circ}$  from nadir). From a flight altitude of 20 km, this IFOV gives a ground sampling distance (spatial resolution) of 20 m for sea level targets and 17 m for surfaces at elevation 3000 m (such as in the San Juan Mountains). A quasi true color image of the 15 June 2011 flight line over SBBBA is shown in Figure 3.

[15] The JPL AVIRIS data facility delivers orthocorrected AVIRIS radiance data with nominal noise-equivalent changes in radiance of  $1.8 \times 10^{-8} \text{ W cm}^{-2} \text{ nm}^{-1} \text{ sr}^{-1}$  at  $\lambda = 700 \text{ nm}$ ,  $2.6 \times 10^{-9} \text{ W cm}^{-2} \text{ nm}^{-1} \text{ sr}^{-1}$  at  $\lambda = 1400 \text{ nm}$ , and  $2.3 \times 10^{-9} \text{ W cm}^{-2} \text{ nm}^{-1} \text{ sr}^{-1}$  at  $\lambda = 2100 \text{ nm}$  (Figure 4). A

geometric lookup table methodology for data rendering employs a 3-D ray tracing and a 30 m spatial resolution digital elevation model [Green, 2012]. The AVIRIS metadata include date/time, flight altitude and heading, and the spectral band centers and full-width half maxima for Gaussian spectral response functions. An overview of the scene-specific parameters used to process the AVIRIS data is provided in Table 1.

#### 3.3. In Situ Data

[16] Among the various measurements at the energy balance and radiation towers in the alpine and subalpine of the SBBBA, they also provide snow albedo [Painter et al., 2007b; Painter et al., 2012b]. These data are collected on an hourly basis and distributed by the Center for Snow and Avalanche Studies (<http://snowstudies.org/>). We use them to validate the AVIRIS albedo retrievals for the particular hour during which acquisitions occurred.

[17] We also retrieve the column water vapor and aerosol optical depth (AOD) from a Cimel Sunphotometer located at the Red Mountain Pass at 3368 m immediately north of the subalpine Swamp Angel Study Plot (SASP) in the SBBBA [Painter et al., 2012b]. This sunphotometer is the Red Mountain Pass site in the NASA Aerosol Robotic Network (AERONET) ([http://aeronet.gsfc.nasa.gov/new\\_web/photo\\_db/Red\\_Mountain\\_Pass.html](http://aeronet.gsfc.nasa.gov/new_web/photo_db/Red_Mountain_Pass.html)). AERONET level 2.0 data between 2005 and 2010 reported annual average AOD of  $0.04 \pm 0.015$  at 500 nm and annual average columnar water vapor of  $0.25 \pm 0.06$  cm.

[18] During the 15 June 2011 flight, we measured spectral solar irradiance and nadir hemispherical-conical reflectance factor (HCRF) [Schaeppman-Strub et al., 2006] of the snow surface with an Analytical Spectral Devices (ASD) FieldSpec3 Max spectroradiometer at the subalpine site in the SBBBA. The FieldSpec3 Max measures reflected radiance and fluxes at wavelengths 350–2500 nm with 3–10 nm full-width half-maximum splined to a spectral output of 1 nm. The noise-equivalent changes in radiance for the ASD FieldSpec3 Max are  $1.1 \times 10^{-9} \text{ W cm}^{-2} \text{ nm}^{-1} \text{ sr}^{-1}$  at  $\lambda = 700 \text{ nm}$ ,  $2.2 \times 10^{-9} \text{ W cm}^{-2} \text{ nm}^{-1} \text{ sr}^{-1}$  at  $\lambda = 1400 \text{ nm}$ , and  $4.0 \times 10^{-9} \text{ W cm}^{-2} \text{ nm}^{-1} \text{ sr}^{-1}$  at  $\lambda = 2100 \text{ nm}$ . The irradiance measurements have laboratory-estimated uncertainties of 2.56% at  $\lambda = 655 \text{ nm}$ , 2.35% at  $\lambda = 1600 \text{ nm}$ , and 3.15% at  $\lambda = 2400 \text{ nm}$  [Analytical Spectral Devices, 2006].



**Figure 3.** Color composite of AVIRIS surface spectral HDRF over San Juan Mountains, on 15 June 2011.

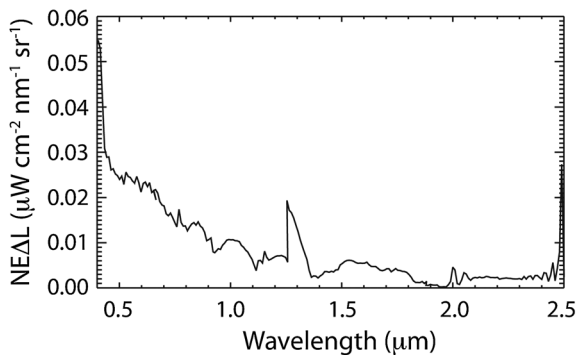


**Figure 4.** AVIRIS spectral noise-equivalent change in radiance ( $\text{NE}\Delta L$ ) (data courtesy of Robert O. Green, Jet Propulsion Laboratory).

#### 4. Retrieval Methods

[19] Here we describe the atmospheric correction of the AVIRIS radiance data and the retrievals of snow grain size, snow albedo, and radiative forcing by LAISI with the IS-SnARF model.

##### 4.1. Atmospheric Compensation and Surface Reflectance

[20] We use the Atmospheric and Topographic Correction for Airborne Imagery (ATCOR-4) software [Richter and Schläpfer, 2011] to retrieve the surface hemispherical-directional reflectance factor  $\text{HDRF}_{sfc}$ :

$$\text{HDRF}_{sfc} = \frac{\pi(L_{\text{AVIRIS}} - L_{\text{atm}})}{\text{T}E_g} \quad (1)$$

where  $L_{\text{AVIRIS}}$  is the at-sensor radiance of AVIRIS,  $L_{\text{atm}}$  is the radiance component of  $L_{\text{AVIRIS}}$  scattered from the atmosphere,  $\text{T}$  is the ground-to-sensor atmospheric transmission, and  $E_g$  is the at-surface irradiance. We assume  $\text{HDRF} \approx \text{HCRF}$  due to the 1 mrad IFOV of the AVIRIS instrument [Schaeppman-Strub *et al.*, 2006].

[21] ATCOR-4 is based on lookup tables created by the Moderate Resolution Atmospheric Transmission (MODTRAN® 5) radiative transfer code, accounting for the influence of the terrain by calculating pixelwise the slope and aspect, as well as the sky-view factor. In this work, we employed a digital elevation model from the U.S. Geological Survey GTOPO30 global elevation data set. See Richter and Schläpfer [2011] for further details on ATCOR-4.

[22] We use the MODTRAN “rural” aerosol model with mixing of 70% small water-soluble and 30% large dust-like particles in the planetary boundary layer and a tropospheric

**Table 1.** Scene Parameters for the 15 June 2011 AVIRIS Data

Date	15 June 2011
Pixel size	$\sim 17$ m at 3000 m elevation
Aerosol optical depth (550 nm)	$0.06 \pm 0.02$ m full scene, 0.05 at SASP
Precipitable water vapor	$0.005 \pm 0.002$ m full scene, 0.0038 at SASP
Mean ground elevation	$3196 \pm 1100$ m
Flight altitude	$20,216 \pm 70$ m
Flight heading	$180 \pm 0.1$

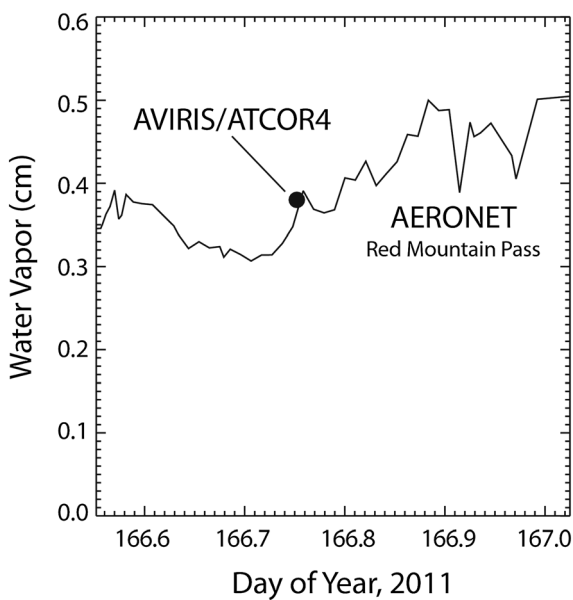


**Figure 5.** Water vapor and aerosol optical depth at 500 nm wavelength from Red Mountain Pass AERONET site on 15 June 2011 and the ATCOR-4 at the AERONET site pixel.

type with 100% small water-soluble particles in the free troposphere. We assume that the uncertainty introduced by the fixed aerosol model is relatively small due to the relatively low aerosol optical depth observed by the AERONET Sun photometer.

#### 4.2. Snow Cover

[23] The determination of snow-covered pixels is carried out using the normalized difference snow index [Dozier and Marks, 1987; Hall *et al.*, 1995]:

$$\text{NDSI} = \frac{\text{HDRF}_{0.6\mu\text{m}} - \text{HDRF}_{1.5\mu\text{m}}}{\text{HDRF}_{0.6\mu\text{m}} + \text{HDRF}_{1.5\mu\text{m}}} \quad (2)$$

where we assume  $\text{NDSI} > 0.9$  as snow covered. We do not increase the computation expense by performing the more intensive fractional snow cover retrieval from the Multiple Endmember Snow Covered Area and Grain Size model [Painter *et al.*, 2003b], because pixels at  $\sim 17$  m are far more homogeneous than at the scale of the 500 m MODIS surface reflectance [Painter *et al.*, 2009].

#### 4.3. Retrieval of Snow Grain Size

[24] We invert the retrieved AVIRIS HDRF<sub>sfc</sub> for snow optical grain size using a new method derived from the Nolin-Dozier approach [Nolin and Dozier, 2000]. We search for the best fit between a modeled clean snow spectrum and the AVIRIS observed HDRF<sub>sfc</sub><sup>obs</sup> at the ice absorption features centered at  $\lambda \cong 1.03 \mu\text{m}$ :

$$r : (\min | \sum_{i=1.03\mu\text{m}}^{1.06\mu\text{m}} \text{HDRF}_{sfc}^{mdl}(\theta_0, \theta_v, \phi_0 - \phi_v; r; \lambda_i) - \text{HDRF}_{sfc}^{obs}(\theta_0, \theta_v, \phi_0 - \phi_v; r; \lambda_i) | ) \quad (3)$$

where  $\theta_{[0,v]}$  denotes the zenith angles for the solar (0) and viewing (v) directions,  $\phi_0 - \phi_v$  is the relative azimuth,  $r$  is

optical grain radius (snow grain size), and  $\lambda$  is the wavelength. We retrieve the snow grain size from the spectral range of 1.03–1.06  $\mu\text{m}$  where the reflected light is primarily sensitive to the snow grain size and less by liquid water and water vapor, which can have severe impacts on reflectance retrieval. Also, implicit in this retrieval is the assumption that the topographic correction is performed correctly. The robustness of reflectance retrievals (described below) supports this assumption.

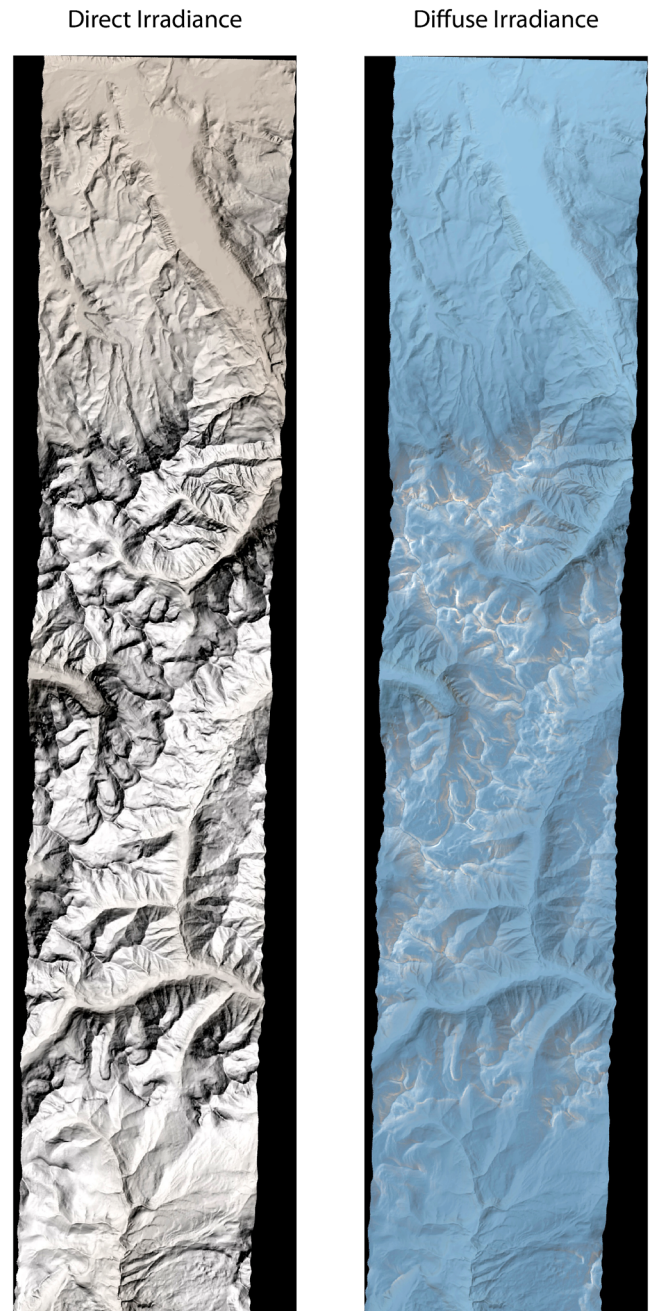


**Figure 6.** Spatial distribution of spectral irradiances estimated by ATCOR-4 for SBBSA AVIRIS acquisition, on 15 June 2011. (a) Color composite of direct irradiances: 638  $\mu\text{m}$  (red), 550  $\mu\text{m}$  (green), and 363  $\mu\text{m}$  (blue). (b) Color composite of diffuse irradiances: 638  $\mu\text{m}$  (red), 550  $\mu\text{m}$  (green), and 363  $\mu\text{m}$  (blue).

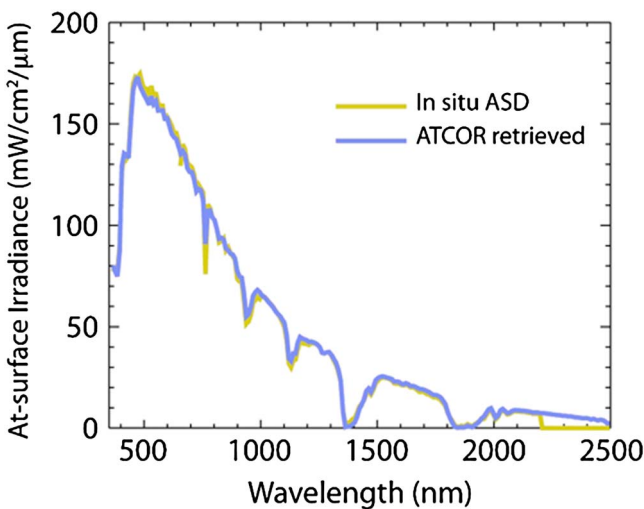


**Figure 7.** Spectral irradiance measured at the Swamp Angel Study Plot in the SBBSA on 15 June 2011 and coincident in situ measurement with the ASD FieldSpec3 Max spectroradiometer and modeled with ATCOR-4.

[25]  $\text{HDRF}_{\text{sfc}}^{\text{mdl}}$  is derived from Mie single scattering calculations [Mie, 1908] and the Discrete Ordinates Radiative Transfer model (DISORT) [Stamnes et al., 1988; Painter et al., 2003b] for monodispersions of ice spheres of grain radius from 10 to 1100  $\mu\text{m}$  by 10  $\mu\text{m}$  intervals. Calculations with monodispersions of spheres can result in spectral ripples [Bohren and Huffman, 1998]; however, in these calculations, ripples only appear in the spectral HDRF and spectral albedo for  $r_e < 40 \mu\text{m}$ , distinctly smaller than snow grain sizes [Painter et al., 1998; Painter et al., 2003b]. Moreover, actual size distributions cannot be known a priori, and thus, monodispersions are used. The  $e$ -folding distance of irradiance into snow (the depth at which the irradiance has been reduced by a factor of  $\frac{1}{e}$ ) at wavelength 1.03  $\mu\text{m}$  is  $\sim 3 \text{ cm}$  for a snow grain radius of 600  $\mu\text{m}$  and density of 500  $\text{kg m}^{-3}$ .

[26] The Nolin/Dozier model has a grain diameter uncertainty of  $\pm 20\text{--}50 \mu\text{m}$  across the grain radius range of 50–900  $\mu\text{m}$  [Nolin and Dozier, 2000]. The present model's uncertainties should be similar to those of Nolin/Dozier but have not been evaluated yet with field measurements of grain size from microtomography or stereology. Here we assume they have similar uncertainties, although preliminary testing suggests that the new technique could be less sensitive to biases due to liquid water and water vapor.

#### 4.4. Snow Albedo

[27] Albedo retrievals are the key to understanding the net shortwave flux to snow, which in most settings modulates snow warming and melt. Unfortunately, airborne and spaceborne instruments lack hemispherical measurements and therefore cannot measure the entire hemisphere-reflected flux to determine albedo [Schaepman-Strub et al., 2006].

[28] We therefore must convert  $\text{HDRF}_{\text{sfc}}^{\text{mdl}}$  to albedo by applying the modeled spectral relationships between directional reflectance factors and albedo ( $\alpha$ ), often referred to as the anisotropy factor:

$$c_{\theta_r, \phi_0 - \phi_v, r; \lambda} = \frac{\alpha_{\text{sfc}}^{\text{mdl}}(r; \lambda)}{\text{HCRF}_{\text{sfc}}^{\text{mdl}}(\theta_0, \theta_v, \phi_0 - \phi_v; r; \lambda)} \quad (4)$$

[29] We apply the scalar  $c$  as a function of the local geometry between solar and observation geometry as well as snow grain size (as determined above) to approximate the spectral surface albedo with

$$\begin{aligned} \alpha_{\text{sfc}}^{\text{obs}}(r; \lambda) \\ = \text{HCRF}_{\text{sfc}}^{\text{obs}}(\theta_0, \theta_v, \phi_0 - \phi_v; r; \lambda) \cdot c_{\theta_r, \phi_0 - \phi_v, r; \lambda} \end{aligned} \quad (5)$$

[30] Implicit in this method is that the presence of dust in the near-surface layers of the snowpack does not modify the ratios between the spectral HDRF<sub>sfc</sub> of snow and the spectral albedo. We do not have the measurements nor have we performed the modeling to test this assumption. A field intensive study with a goniometer such as the Automated Spectro-Goniometer [Painter et al., 2003a] or Field Goniometer System [Sandmeier and Itten, 1999] in a setting such as the dust-influenced mountains of the Upper Colorado River Basin would address this uncertainty.

[31] From the spectral albedo and the spectral irradiances, we can then determine the spectrally integrated broadband albedo:

$$\alpha_{\text{sfc}}^{\text{obs}}(r) = \frac{\sum_{\lambda=0.35 \mu\text{m}}^{2.50 \mu\text{m}} E(\lambda; \theta_0) \cdot \alpha_{\text{sfc}}^{\text{obs}}(r; \lambda) \Delta\lambda}{\sum_{\lambda=0.35 \mu\text{m}}^{2.50 \mu\text{m}} E(\lambda; \theta_0) \Delta\lambda} \quad (6)$$

where  $E(\lambda; \theta_0)$  denotes the spectral irradiance ( $\text{W m}^{-2} \mu\text{m}^{-1}$ ) and  $\Delta\lambda$  is the full width at half maximum of each AVIRIS band pass (generally Gaussian spectral response functions).

#### 4.5. Retrieval of LAISI Radiative Forcing

[32] In order to determine the radiative forcing by LAISI, we must first determine the spectral albedo of clean snow of the same optical grain radius as the observed snow. The model first infers the snow grain size from the ice absorption

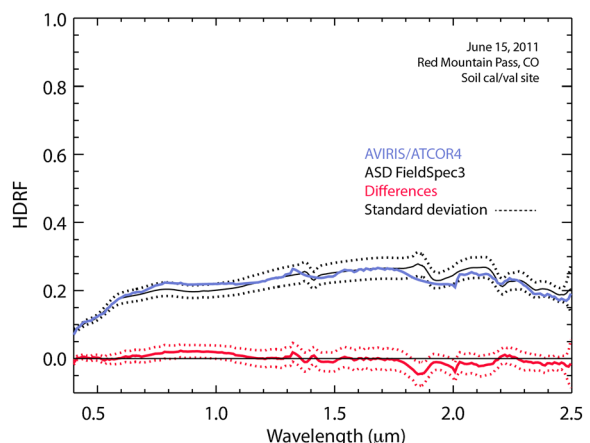


**Figure 8.** Spectral surface HDRF validation at soil validation target. AVIRIS/ATCOR-4 on 15 June 2011 and in situ with ASD field spectroradiometer.

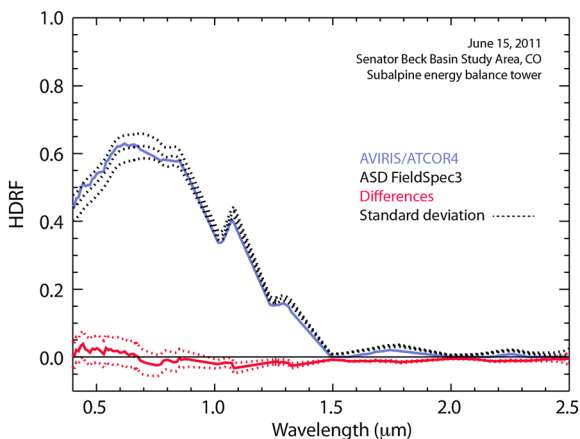


**Figure 9.** Snow spectral surface HDRF from AVIRIS/ATCOR-4 and in situ at Swamp Angel Study Plot, on 15 June 2011.

feature at  $1.03\text{ }\mu\text{m}$ , as described above.

[33] The radiative forcing is then determined from the convolution of the spectral irradiance with the spectral difference between the model spectra of a clean snow albedo  $\alpha_{sfc}^{mdl}$  and the observed snow spectral albedo  $\alpha_{sfc}^{obs}$  for each AVIRIS pixel (from equation (5)):

$$RF = \sum_{\lambda=0.36\text{ }\mu\text{m}}^{1.00\text{ }\mu\text{m}} E(\theta_0; \lambda) \cdot (\alpha_{sfc}^{mdl}(\lambda; r) - \alpha_{sfc}^{obs}(\lambda; r)) d\lambda \quad (7)$$

[34] The choice of  $1.00\text{ }\mu\text{m}$  as the upper limit of integration is selected somewhat arbitrarily based on the longer wavelength end at which we expect radiative forcing to occur from LAISI. However, the combination of relatively small divergence of  $\alpha$  in these longer wavelengths and markedly lower irradiances than in the visible wavelengths makes this choice robust.

## 5. Results

[35] Below we present the retrievals and comparisons with in situ observations of AOD, water vapor, irradiance, spectral HDRF, snow grain size, snow albedo, and radiative forcing by LAISI.

### 5.1. Aerosol Optical Depth and Water Vapor

[36] AOD is prescribed in ATCOR-4 through the establishment of the visibility at a given elevation. The Red Mountain Pass AERONET site retrieved an AOD at 500 nm wavelength of 0.04 at the time of acquisition, which gives an effective visibility of greater than 100 km. Therefore, we set the ATCOR-4 visibility to 100 km, which is the maximum visibility in the model. ATCOR-4 then distributes AOD according to elevation by the relationship:

$$AOD(z, VIS) = \exp(a(z) + b(z) \cdot \ln(VIS)) \quad (8)$$

where  $z$  is the surface elevation and  $a(z)$  and  $b(z)$  are the coefficients from linear regression of  $\ln(AOD)$  versus  $\ln(VIS)$ , calculated from MODTRAN5.

[37] ATCOR-4 leverages the AVIRIS spectrum to also retrieve column water vapor (cm precipitable water). The AVIRIS/ATCOR-4 water vapor retrieval across the scene

was  $0.55 \pm 0.25\text{ cm}$ . The AVIRIS-retrieved water vapor was  $0.39\text{ cm}$  for the  $3 \times 3$  pixel column centered above the AERONET Red Mountain Pass sunphotometer, and the AERONET retrieved column water vapor was  $0.37\text{ cm}$  (Figure 5).

### 5.2. Irradiance at the Surface

[38] In the course of the atmospheric compensation, ATCOR-4 must determine the per-pixel, at-surface spectral irradiances. We have worked with the ATCOR-4 team to allow irradiances to be output as their spectral direct and spectral diffuse components (Figure 6). The direct component is modulated primarily by the topography and reduced at lower elevations due to atmospheric attenuation. The diffuse component is less sensitive to the topography and increases in magnitude at lower elevations due to atmospheric scattering.

[39] We validate these retrievals of spectral irradiance with coincident in situ measurements from the ASD FieldSpec3 Max spectroradiometer described above (Figure 7). The ATCOR-4-calculated spectral irradiance differs from the ASD-measured spectral irradiance with a mean of  $0.2\text{ mW cm}^{-2}\text{ }\mu\text{m}^{-1}$ , standard deviation of  $2.3\text{ mW cm}^{-2}\text{ }\mu\text{m}^{-1}$ , and a range of errors across the spectrum of  $-6.2$  to  $14.9\text{ mW cm}^{-2}\text{ }\mu\text{m}^{-1}$ . When integrated spectrally, the ATCOR-4 irradiance is  $1052\text{ W m}^{-2}$  compared to  $1048\text{ W m}^{-2}$  from the ASD measurement, an absolute difference of  $4\text{ W m}^{-2}$  and relative difference of  $0.4\%$ .

### 5.3. Spectral HDRF

[40] Our first evaluation of the ATCOR-4 retrieval of  $HDRF_{sfc}$  comes at a soil parking area on the south side of Red Mountain Pass with ground spectra measured with the ASD FieldSpec3 Max. The validation site was characterized with 100 spectra acquired throughout the site. We compare the AVIRIS/ATCOR-4 spectrum with the mean, median, and mean  $\pm 1$  standard deviation of the 100 ASD spectra from the site (Figure 8). The mean difference across the spectrum was  $-0.002$ , and the root-mean-square error was  $0.015$ .

[41] To assess the retrieval of the snow  $HDRF_{sfc}$ , we perform a similar comparison between the ATCOR-4 retrieval and in situ ASD measurements at the Swamp Angel Study Plot (SASP) (Figure 9). The ASD measurements were made along a transect near the subalpine tower at the time of overflight and averaged to the mean spectrum presented in the figure, along with the standard deviation. The mean  $HDRF_{sfc}$  difference across the spectrum was  $-0.006$ , and the spectrum root-mean-square error was  $0.014$ , relatively close to those for the soil calibration site. Across the spectrum from  $\sim 0.9\text{ }\mu\text{m}$  to greater, the AVIRIS  $HDRF_{sfc}$  is lower than the observations in the field but by  $<0.015$ .

### 5.4. Snow Grain Size

[42] In Figure 10a, we present the spatial distribution of snow grain size retrieved from the  $1.03\text{ }\mu\text{m}$  ice absorption feature. This turns out to hold what seems to be a counterintuitive result. Across the lower elevations, near-surface snow grain size increases with elevation, whereas we generally expect that in sustained warmer conditions at lower elevation, the grain size would be larger. The interaction with radiative forcing is discussed in section 5.7 below. Grain sizes at the lower elevations are  $\sim 500\text{ }\mu\text{m}$  but rise to level

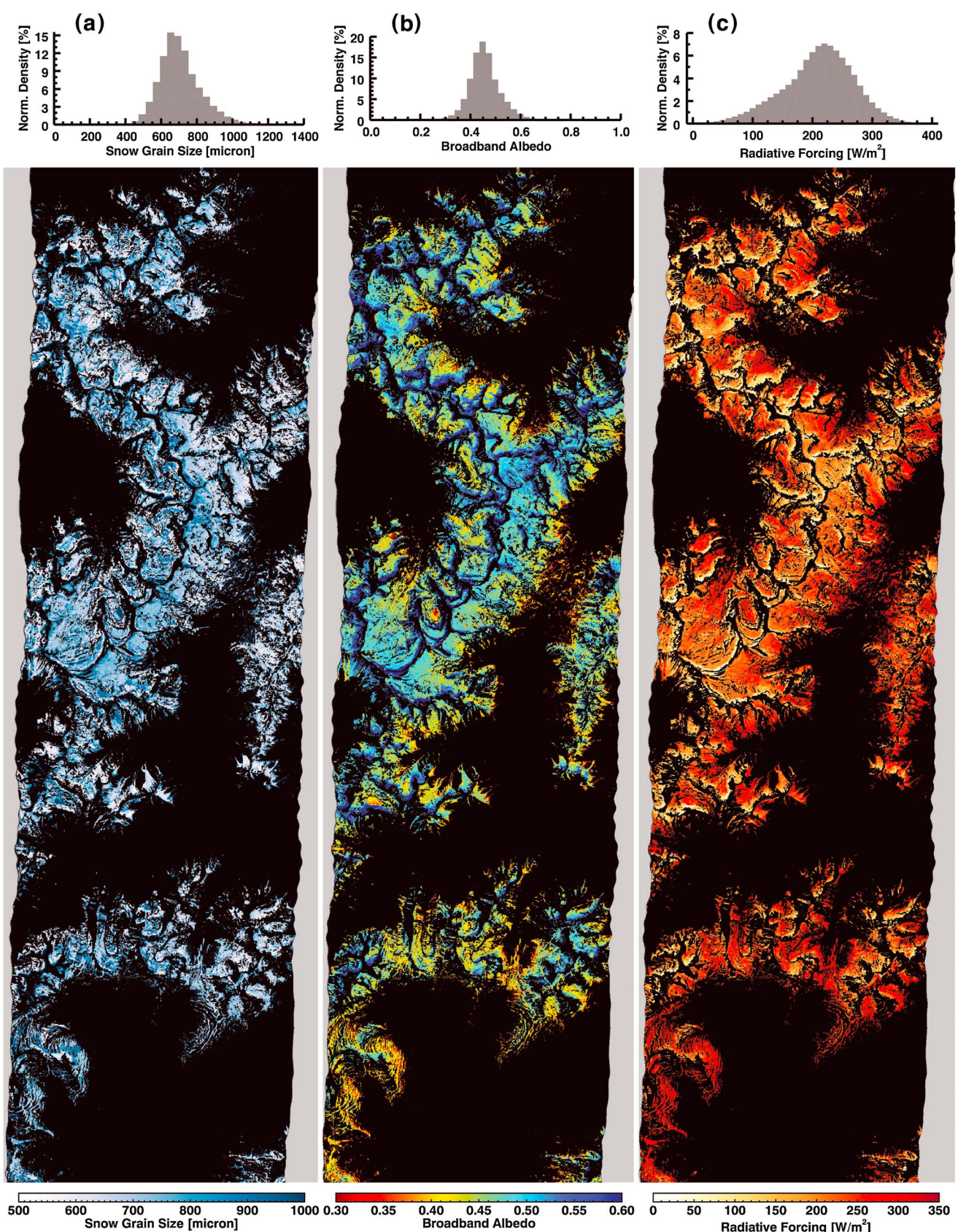


**Figure 10.** Spatial distribution of (a) snow grain radius, (b) spectrally integrated snow albedo, and (c) LAISI radiative forcing in snow, on 15 June 2011.

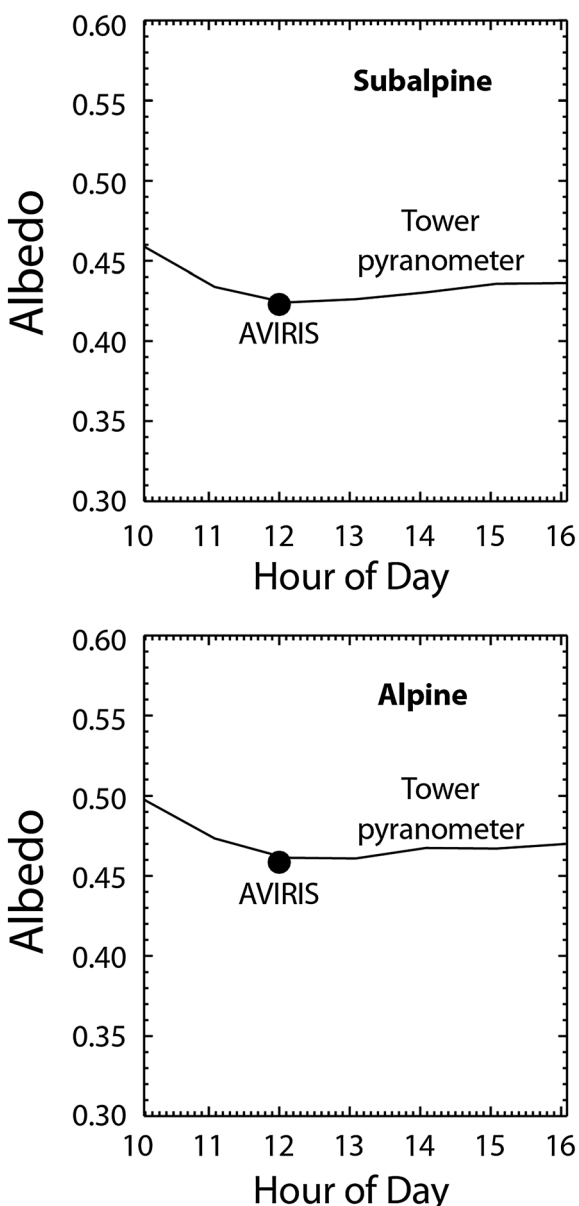


**Figure 11.** Surface albedo from energy balance/radiation towers and AVIRIS in subalpine (top) and alpine (bottom).

off at  $\sim 750 \mu\text{m}$ . Overall, the mean grain size across the scene was  $732 \mu\text{m}$  with a standard deviation of  $223 \mu\text{m}$ .

[43] The impact of errors in grain size proliferates into the retrieval of radiative forcing by LAISI but not directly that of spectral albedo or spectrally integrated albedo, which is determined from the AVIRIS reflectance spectrum directly. However, the grain size retrieval is used to determine the anisotropy factor (equation (4)), and in turn, the uncertainties in grain size have a minor impact on the albedo retrieval (discussed below).

### 5.5. Snow Spectrally Integrated Albedo

[44] The snow albedo retrieval is shown in Figure 10b. Despite the fact that snow grain size increases with elevation in some regions (which would presumably make albedo decrease), snow albedo still increases with elevation due to

the drop in LAISI exposure. Mean snow albedo in this scene was 0.47 with a range of 0.27–0.67 and a standard deviation of 0.07. The distribution is roughly Gaussian with a slight skew toward larger albedo.

[45] Validation of the AVIRIS albedo retrieval at the Senator Beck Basin alpine and subalpine energy balance and radiation towers shows robust retrievals, against the daylight hour pyranometer retrievals (Figure 11). At the alpine site, the daylight albedos range from 0.46 to 0.50, whereas at the lower elevation subalpine site, the daylight albedos range from 0.42 to 0.46. These bowl-shaped variations in snow albedo are due to the strong forward scattering by ice particles, which forces albedo to be higher at larger solar zenith angles [Warren, 1982]. The mean AVIRIS-retrieved albedo in the 3 by 3 window around the pixel containing the alpine tower was 0.463, coincident with in situ observation of 0.459. At the subalpine tower, the mean AVIRIS-retrieved albedo was 0.424 and in situ observation of 0.423. Therefore, our best understanding of the uncertainty in albedo retrieval is 0.001–0.004.

[46] Consistent with lower aspect-averaged energy fluxes at higher elevations and recent snowfall, the albedo increases with elevation (Figure 12a). Moreover, albedo tends to be higher on north facing slopes at the highest elevations where energy fluxes are lowest. Albedos tend to be lowest on the east to south aspects (Figure 12b).

### 5.6. LAISI Radiative Forcing

[47] The spatial distribution of radiative forcing by LAISI is presented in Figure 10c. As suggested by the color composite in Figure 3, radiative forcing by LAISI was greater at lower elevations. Radiative forcings ranged from 0 to  $400 \text{ W m}^{-2}$ , with a mean of  $215 \text{ W m}^{-2}$  and standard deviation of  $63 \text{ W m}^{-2}$ . We compared the AVIRIS radiative forcing retrievals with those from the ground-based field spectrometer retrievals near the subalpine tower. The AVIRIS radiative forcing errors were  $2.1 \pm 5.1 \text{ W m}^{-2}$  against the ground-observed mean radiative forcing of  $300 \text{ W m}^{-2}$ .

[48] The AVIRIS data were acquired at  $\sim$ GMT18:00 when the solar zenith angle was  $20.2^\circ$ , relative to a solar noon zenith angle of  $14.5^\circ$ . The ratio of cosines  $\cos(20.2^\circ)/\cos(14.5^\circ) = 0.938/0.968 = 0.97$ . That is, for the direct irradiances on level terrain, these were sampled when direct irradiances were 97% of peak daily irradiance. Daily mean radiative forcing would be determined through a diurnal calculation of irradiances across all terrain facets, beyond the scope of this paper.

[49] The lowest radiative forcings lie in the high north facing cirques where energy fluxes are lower, metamorphism is slower, and relatively recent, cleaner snow fall remains longer (Figure 12d). The highest radiative forcings lie on southeast facing slopes at the lowest elevations where snow remains (Figure 12c).

[50] We can now determine the extra mass of snow that was melted during the hour in which the AVIRIS data were acquired. We know from the tower observations that the imaged snowpack had a temperature of  $0^\circ\text{C}$ , and therefore, none of the radiative forcing went to reducing snow cold content (that is, the energy necessary to bring the snow column to  $0^\circ\text{C}$ ).

[51] With the enthalpy of fusion of water at  $0^\circ\text{C}$  of  $0.334 \times 10^6 \text{ J kg}^{-1}$ , the radiative forcing of  $338 \text{ W m}^{-2}$  at the subalpine tower across the hour during acquisition translates into  $3.6 \text{ kg m}^{-2}$  of melt, or 4 mm of snow water equivalent. The mean melt rate from the radiative forcing by LAISI

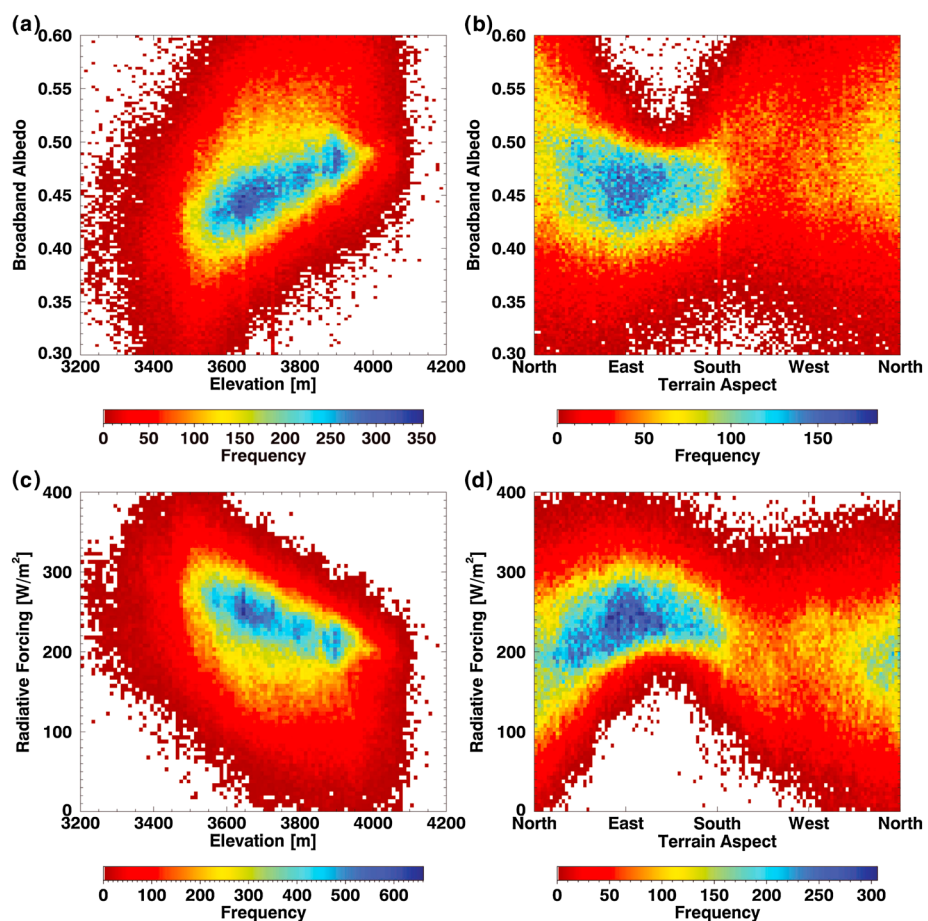


**Figure 12.** Variation of broadband albedo and radiative forcing with terrain aspect and elevation. Each plot shows a two-dimensional histogram with bin sizes of 0.0025 for albedo,  $5 \text{ W m}^{-2}$  for radiative forcing,  $3^\circ$  for aspect, and 10 m for elevation. (a) Albedo versus aspect. (b) Albedo versus elevation. (c) Radiative forcing versus aspect. (d) Radiative forcing versus elevation.

across the 14 h of nonzero irradiance is  $\sim 2 \text{ mm/h}$  or 26 mm of the subalpine SWE of 450 mm, atop the absorption by coarse grain snow in the absence of those absorbers. Just the radiative forcing by LAISI would melt away the snowpack in 17 days.

[52] At the alpine site, the radiative forcing of  $240 \text{ W m}^{-2}$  translates into  $2.6 \text{ kg m}^{-2}$  of melt or 3 mm of snow water equivalent. Across the 14 h of irradiance, the mean melt rate is  $1.5 \text{ mm/h}$ , giving a daily melt from radiative forcing of 18 mm of the alpine SWE of 503 mm.

### 5.7. Uncertainties

[53] We now determine the uncertainties in retrievals due to the AVIRIS noise-equivalent changes in radiance ( $\text{NE}\Delta L$ , Figure 4). The greatest  $\text{NE}\Delta L$  comes in the blue end of the

spectrum, which coincides with the wavelengths in which the radiative forcing by LAISI in snow is most pronounced. We passed the spectral  $\text{NE}\Delta L$  through the retrieval chain of atmospheric compensation retrievals of water vapor, grain size, albedo, and radiative forcing by retrieving all of these with the measured radiance perturbed  $\pm \text{NE}\Delta L$  (Table 2).

[54] The uncertainty in retrieving column water vapor due to the AVIRIS spectral  $\text{NE}\Delta L$  was  $\pm 0.0007 \text{ cm}$ . For grain size retrievals, the uncertainties are  $\pm 3.6 \mu\text{m}$ . For albedo retrievals, the uncertainty is  $\pm 0.001$ , and for instantaneous radiative forcing, it is  $0.2 \text{ W m}^{-2}$ .

[55] The grain size retrieval has an assumed uncertainty of  $\pm 25 \mu\text{m}$  in radius at the smaller grain sizes here [Nolin and Dozier, 2000]. We passed this uncertainty through the retrieval of albedo and radiative forcing, the latter of which depends on

**Table 2.** Sensitivity of Retrievals to AVIRIS Noise-Equivalent Change in Radiance ( $\text{NE}\Delta L$ )

Retrieval	Uncertainty From $\text{NE}\Delta L$
Water vapor	$\pm 0.0007 \text{ cm}$
Snow grain radius ( $1.03 \mu\text{m}$ )	$\pm 3.6 \mu\text{m}$
Snow albedo (range, 0–1)	$\pm 0.001$ (unitless)
LAISI radiative forcing in snow	$\pm 0.2 \text{ W m}^{-2}$
Correction factor for RF spectrum	$\pm 0.003$ (unitless)

**Table 3.** Sensitivity of Retrievals to Snow Grain Size Uncertainty of  $\pm 25 \mu\text{m}$

Retrieval	Uncertainty From Snow Grain Size
Snow albedo (range, 0–1)	$\pm 0.0001$ (unitless)
LAISI radiative forcing in snow	$\pm 3.8 \text{ W m}^{-2}$

the retrieval of grain size for the associated clean snow spectral albedo (Table 3). Moreover, the spectral albedo is affected by the grain size uncertainty through the grain size-dependent selection of the anisotropy factor. The uncertainties in snow albedo from uncertainty in grain size are  $\pm 0.0001$  (unitless), and the uncertainties in LAISI radiative forcing from grain size uncertainty are  $\pm 3.8 \text{ W m}^{-2}$ .

[56] Regarding grain size stratigraphy impact on retrievals, while it is true that stratigraphy can affect radiative forcing, it is a relatively minor issue. *Beaglehole et al.* [1998] and *Perovich* [2007] show that transmission in the visible wavelengths drops to  $\sim 10\%$  by 2 cm into the snowpack and to  $\sim 2\%$  by 5 cm into the snowpack. Therefore, for clean snow, nearly 90% of the visible irradiance is scattered in the top 2 cm. When a dirty layer is at the snow surface, the near-surface absorption of visible irradiance is dramatically increased and the penetration of irradiance is further reduced. Nevertheless, further studies would help inform this precisely.

[57] Moreover, as we move toward shorter wavelengths, the clean snow spectral albedo is less sensitive to grain size, especially in the visible wavelengths where the impurities have their largest impact and the spectral irradiance is the greatest. So if there is considerable variation in grain size in the top 30 cm or so of the snow column, it is already manifested by the hemispherical flux that has been sampled with a narrow conical field of view from the sensor. The issue then would have to come between the visible wavelengths and  $1.03 \mu\text{m}$ —how divergent is the selected clean snow spectral albedo in those wavelengths? Because it is well anchored in the visible wavelengths and it is well anchored at  $1.03 \mu\text{m}$ , the divergence should be small. A modeling study on the variation of spectral albedo of clean and impurity-laden snow with variation in snow grain size stratigraphy would be worthwhile to test the above conjecture.

[58] Finally, as mentioned before, we assume that the relationship between the directional reflectance and albedo for snow with light-absorbing impurities is the same as that for clean snow. We know that the relationship for clean snow spheres itself is not identical to that for actual snow; however, as snow grains grow in size and become more spherical, this assumption becomes more valid [*Painter and Dozier*, 2004]. However, we do not yet know how impurities modify the relationship between directional reflectance and albedo. The intensive snowmelt and percolation of meltwater that we have observed suggest that modeling the above would be challenging and instead would demand measurements with a goniometer with spectrometer [*Sandmeier and Itten*, 1999; *Painter et al.*, 2003a].

## 6. Discussion

[59] The LAISI and climate communities are strongly interested in knowing not only the spatial distribution of radiative forcing but also the spatial distribution of LAISI concentrations in the near-surface layers. We do not yet have such retrievals because we lack the capacity to know the LAISI size distribution and optical properties (spectral complex refractive index) from remotely sensed data. However, with regional knowledge of the LAISI size distribution and optical properties to constrain the radiative transfer modeling, we could invert for concentration of LAI. In the case of the San Juan Mountains, Colorado, USA, for example, we

know that the size distribution of LAISI is relatively stable from deposition event to deposition event based on the work of *Lawrence et al.* [2010]. Remaining to determine will be the spectral complex refractive index of the LAISI. The Snow Optics Laboratory, JPL is currently working on techniques for these inversions with colleagues.

[60] As discussed above, in some regions, grain size increased with elevation, whereas LAISI radiative forcing decreased with elevation. The general understanding is that the direct effect of LAISI radiative forcing leads to increases in snow grain size and a further reduction of snow albedo (the first feedback) [*Hansen and Nazarenko*, 2004]. Indeed, *Painter et al.* [2003b] found with AVIRIS data from the Sierra Nevada, California, a decrease in grain size with an increase in elevation. The result presented here is inconsistent with that concept. However, the lead author has been observing this apparent inconsistency for several years in the Senator Beck Basin from ASD spectrometer measurements and contact spectroscopy profiles [*Painter et al.*, 2007a] under conditions of intense dust loading and radiative forcing.

[61] The grain size stratigraphies shown in *Painter et al.* [2007a] indicate that dusty snowpacks show distinctly smaller grain sizes immediately at the surface, whereas at 2–10 cm, at depth in the snowpack where snowmelt infiltration reaches and refreezes, grain radii are 100–200  $\mu\text{m}$  greater. We know from our field observations that dust layers dramatically generate or accelerate melt and lead to grain coarsening. However, this grain coarsening appears to occur at depth as melt percolates vertically, leaving behind a near-surface layer of smaller grains.

[62] These results suggest that the intensification of snowmelt by dust in the visible wavelengths results in destructive metamorphism of snow grains near the snow-atmosphere interface, resulting in smaller grain sizes at the surface. With smaller grain sizes at the near surface, the near-infrared/shortwave infrared ( $0.75\text{--}2.5 \mu\text{m}$ ) albedo then increases, mitigating to a degree the absorption of shortwave irradiance across the rest of the spectrum. Therefore, the conceptual model of *Hansen and Nazarenko* [2004] and others that the direct effect of radiative forcing gives the first feedback of decreased albedo from grain coarsening would be correct if the snowmelt infiltration and coarsening did not happen at depth in the pack beyond the dominant access of sunlight. The seasonality of the grain size/albedo feedback to radiative forcing from LAISI should therefore be further explored.

[63] Where snowpack is relatively thin but clean, visible irradiance can penetrate to a darker substrate and present a spectral albedo that is similar to that of snow with impurities [*Warren*, 1982]. Therefore, an error can occur in these regions. However, mountain snow cover does not tend to have broad expanses of thin snow, whereas polar tundra can [*Warren*, 2013]. In the coming year, the coincident snow depth measurement from lidar on the Jet Propulsion Laboratory's Airborne Snow Observatory will accompany its imaging spectrometer's measurements and provide masking of thin snow and mixed pixels from radiative forcing retrievals. Likewise, thin clouds and blowing snow can present retrieved reflectance signatures that appear like impurity-laden snow, but again, these are far more episodic in mountain systems than in polar regions.

[64] Studies of the damaging health impacts of anthropogenic aerosols (e.g., black carbon, brown carbon, etc.) and

minimal observations have led to calls for reductions in emissions from the United Nations Environment Programme [UNEP/WMO, 2011], the Vatican's Pontifical Academy of Sciences [Sciences, 2011], and the U.S. Department of State's initiation of the Climate and Clean Air Coalition to Reduce Short-Lived Climate Pollutants. As these regional to global political efforts to reduce short-lived pollutants become more likely to affect change in magnitude of emissions, it is critical that we monitor the current temporal and spatial dynamics in order to understand the efficacy of these treatments. The algorithm presented here is directly applicable to airborne (e.g., AVIRIS and Airborne Prism Experiment-APEX) and spaceborne imaging spectrometer data (e.g., the NASA Decadal Survey mission Hyperspectral Infrared Imager-HypSIRI) to retrieve and map these parameters on local to regional scales in mountainous and arctic regions to inform scientific discoveries and policy decisions and agreements.

[65] **Acknowledgments.** This work was funded by the National Science Foundation grant ATM0432327 and NASA project NNX10AO97G. Part of this work was performed at the Jet Propulsion Laboratory, California Institute of Technology, under a contract with NASA.

## References

- Analytical Spectral Devices (2006), Analytical Spectral Devices, Inc., <http://www.asdi.com/>.
- Beaglehole, D., B. Ramanathan, and J. Rumberg (1998), The UV to IR transmittance of Antarctic snow, *J. Geophys. Res.*, **103**, 8849–8857.
- Bohren, C. F., and D. R. Huffman (1998), *Absorption and Scattering of Light by Small Particles*, 530 pp., John Wiley, New York.
- Conway, H., A. Gades, and C. F. Raymond (1996), Albedo of dirty snow during conditions of melt, *Water Resour. Res.*, **32**, 1713–1718, doi:10.1029/96WR00712.
- Davityan, F. F. (1968), Atmospheric dust content as a factor affecting glaciation and climatic change, *Ann. Assoc. Am. Geogr.*, **59**, 552–560.
- Dozier, J., and D. Marks (1987), Snow mapping and classification from Landsat Thematic Mapper data, *Ann. Glaciol.*, **9**, 97–103.
- Green, R. O. (2012), AVIRIS homepage, Jet Propulsion Laboratory/California Institute of Technology, <http://aviris.jpl.nasa.gov/>.
- Hall, D. K., G. A. Riggs, and V. V. Salomonson (1995), Development of methods for mapping global snow cover using Moderate Resolution Imaging Spectroradiometer data, *Remote Sens. Environ.*, **54**, 127–140.
- Hansen, J., and L. Nazarenko (2004), Soot climate forcing via snow and ice albedos, *Proc. Natl. Acad. Sci. U. S. A.*, **101**, 423–428, doi:10.1073/pnas.0223715100.
- Higuchi, K., and A. Nagoshi (1977), Effect of particulate matter in surface snow layers on the albedo of perennial snow patches, in *Isotopes and Impurities in Snow and Ice*, edited by J. F. Nye, F. Miller, and H. Oeschger, *IAHS AISH Publ.*, **118**, 95–97.
- Kaspari, S. D., M. Schwikowski, M. G. Flanner, S. Kang, S. Hou, and P. A. Mayewski (2011), Recent increase in black carbon concentrations from a Mt. Everest ice core spanning 1860–2000 AD, *Geophys. Res. Lett.*, **38**, L04703, doi:10.1029/2010GL046096.
- Lau, W. K. M., M.-K. Kim, K.-M. Kim, and W.-S. Lee (2010), Enhanced surface warming and accelerated snow melt in the Himalayas and Tibetan Plateau induced by absorbing aerosols, *Environ. Res. Lett.*, **5**, doi:10.1088/1748-9326/5/2/025204.
- Lawrence, C. R., T. H. Painter, and J. C. Neff (2010), Contemporary geochemical composition and flux of aeolian dust to the San Juan Mountains, Colorado, United States, *J. Geophys. Res.*, **115**, G03007, doi:10.1029/2009JG001077.
- McConnell, J. R., A. J. Aristarain, J. R. Banta, P. R. Edwards, and J. C. Simoes (2007), 20th-Century doubling in dust archived in an Antarctic Peninsula ice core parallels climate change and desertification in South America, *Proc. Natl. Acad. Sci. U. S. A.*, **104**, 5743–5748, doi:10.1073/pnas.0607657104.
- Mie, G. (1908), Beiträge zur Optik trüber Medien, Speziell Kolloidaler Metallösungen, *Ann. Phys.*, **25**, 377–445.
- Neff, J. C., A. P. Ballantyne, G. L. Farmer, N. M. Mahowald, J. L. Conroy, C. C. Landry, J. T. Overpeck, T. H. Painter, C. R. Lawrence, and R. L. Reynolds (2008), Increasing eolian dust deposition in the western United States linked to human activity, *Nat. Geosci.*, **1**, 189–195, doi:10.1038/ngeo133.
- Nolin, A. W., and J. Dozier (2000), A hyperspectral method for remotely sensing the grain size of snow, *Remote Sens. Environ.*, **74**, 207–216.
- Oerlemans, J. (2000), Analysis of a 3 year meteorological record from the ablation zone of Morteratsch glacier, Switzerland: Energy and mass balance, *J. Glaciol.*, **46**, 571–579, doi:10.3189/172756500781832657.
- Painter, T. H., D. A. Roberts, R. O. Green, and J. Dozier (1998), The effect of grain size on spectral mixture analysis of snow-covered area from AVIRIS data, *Remote Sens. Environ.*, **65**, 320–332.
- Painter, T. H., B. Paden, and J. Dozier (2003a), Automated Spectro-Goniometer: A spherical-robot for the measurement of the directional reflectance of snow, *Rev. Sci. Instrum.*, **74**, 5179–5188.
- Painter, T. H., J. Dozier, D. A. Roberts, R. E. Davis, and R. O. Green (2003b), Retrieval of subpixel snow-covered area and grain size from imaging spectrometer data, *Remote Sens. Environ.*, **85**, 64–77, doi:10.1016/S0034-4257(02)00187-6.
- Painter, T. H., and J. Dozier (2004), Measurements of the hemispherical-directional reflectance of snow at fine spectral and angular resolution, *J. Geophys. Res.*, **109**, D18115, doi:10.1029/2003JD004458.
- Painter, T. H., N. P. Molotch, M. P. Cassidy, M. G. Flanner, and K. Steffen (2007a), Contact spectroscopy for the determination of stratigraphy of snow grain size, *J. Glaciol.*, **53**, 121–127, doi:10.3189/172756507781833947.
- Painter, T. H., A. P. Barrett, C. C. Landry, J. C. Neff, M. P. Cassidy, C. R. Lawrence, K. E. McBride, and G. L. Farmer (2007b), Impact of disturbed desert soils on duration of mountain snow cover, *Geophys. Res. Lett.*, **34**, L12502, doi:10.1029/2007GL030284.
- Painter, T. H., K. Rittger, C. McKenzie, P. Slaughter, R. E. Davis, and J. Dozier (2009), Retrieval of subpixel snow covered area, grain size, and albedo from MODIS, *Remote Sens. Environ.*, **113**, 868–879, doi:10.1016/j.rse.2009.01.001.
- Painter, T. H., J. S. Deems, J. Belnap, A. F. Hamlet, C. C. Landry, and B. Udall (2010), Response of Colorado River runoff to dust radiative forcing in snow, *Proc. Natl. Acad. Sci. U. S. A.*, **107**, 17,125–17,130, doi:10.1073/pnas.0913139107.
- Painter, T. H., A. C. Bryant, and S. M. Skiles (2012a), Radiative forcing of dust in mountain snow from MODIS surface reflectance data, *Geophys. Res. Lett.*, doi:10.1029/2012GL052457.
- Painter, T. H., S. M. Skiles, J. S. Deems, A. C. Bryant, and C. C. Landry (2012b), Dust radiative forcing in snow of the Upper Colorado River Basin: 1. A 6 year record of energy balance, radiation, and dust concentrations, *Water Resour. Res.*, **48**, W07521, doi:10.1029/2012WR011985.
- Perovich, D. K. (2007), Light reflection and transmission by a temperate snow cover, *J. Glaciol.*, **53**, 201–210, doi:10.3189/172756507782202919.
- Qian, Y., M. G. Flanner, L. R. Leung, and W. Wang (2011), Sensitivity studies on the impacts of Tibetan Plateau snowpack pollution on the Asian hydrological cycle and monsoon climate, *Atmos. Chem. Phys.*, **11**, 1929–1948, doi:10.5194/acp-11-1929-2011.
- Reynolds, R. L., J. S. Mordecai, J. G. Rosenbaum, M. E. Ketterer, M. K. Walsh, and K. A. Moser (2009), Compositional changes in sediments of subalpine lakes, Uinta Mountains (Utah): Evidence for the effects of human activity on atmospheric dust inputs, *J. Paleolimnol.*, **44**, 161–175, doi:10.1007/s10933-009-9394-8.
- Richter, R., and D. Schläpfer (2011), *Atmospheric/Topographic Correction for Airborne Imagery*, 194 pp., DLR, Wessling, Germany.
- Sandmeier, S. R., and K. I. Itten (1999), A field goniometer system (FIGOS) for acquisition of hyperspectral BRDF data, *IEEE Trans. Geosci. Remote Sens.*, **37**, 978–986.
- Schaepman-Strub, G., M. Schaepman, T. H. Painter, S. Dangel, and J. V. Martonchik (2006), Reflectance quantities in optical remote sensing—Definitions and case studies, *Remote Sens. Environ.*, **103**, 27–42.
- Sciences, P. A. o. (2011), *Fate of Mountain Glaciers in the Anthropocene*, 15 pp., Pontifical Acad. of Sci., Vatican City.
- Skiles, S. M., T. H. Painter, J. S. Deems, A. C. Bryant, and C. C. Landry (2012), Dust radiative forcing in snow of the Upper Colorado River Basin: 2. Interannual variability in radiative forcing and snowmelt rates, *Water Resour. Res.*, **48**, W07522, doi:10.1029/2012WR011986.
- Stamnes, K., S.-C. Tsay, W. J. Wiscombe, and K. Jayaweera (1988), Numerically stable algorithm for discrete-ordinate-method radiative transfer in multiple scattering and emitting layered media, *Appl. Opt.*, **27**, 2502–2509.
- Sterle, K. M., J. R. McConnell, J. Dozier, R. Edwards, and M. G. Flanner (2013), Retention and radiative forcing of black carbon in eastern Sierra Nevada snow, *Cryosphere*, **7**, 365–374, doi:10.5194/tc-7-365-2013.
- Thevenon, F., F. S. Anselmetti, S. M. Bernasconi, and M. Schwikowski (2009), Mineral dust and elemental black carbon records from an Alpine ice core (Colle Gnifetti glacier) over the last millennium, *J. Geophys. Res.*, **114**, D17102, doi:10.1029/2008JD011490.

## PAINTER ET AL.: RADIATIVE FORCING DUST/BC IN SNOW

- Thompson, L. G., T. Yao, E. Mosley-Thompson, M. E. Davis, K. A. Henderson, and P.-N. Lin (2000), A high-resolution millennial record of the South Asian monsoon from Himalayan ice cores, *Science*, 289, 1916–1919, doi:10.1126/science.289.5486.1916.
- UNEP/WMO (2011), *Integrated Assessment of Black Carbon and Tropospheric Ozone*, 285 pp., United Nations Environmental Programme, Nairobi, Kenya.
- Warren, S. G. (1982), Optical properties of snow, *Rev. Geophys. Space Phys.*, 20, 67–89.
- Warren, S. G. (2013), Can black carbon in snow be detected by remote sensing? *J. Geophys. Res. Atmos.*, 118, 779–786, doi:10.1029/2012JD018476.
- Zalasiewicz, J., M. Williams, W. Steffen, and P. Crutzen (2010), The new world of the Anthropocene, *Environ. Sci. Technol.*, 44, 2228–2231, doi:10.1021/es903118j.